Prediction of high-pressure polymorphism in NiS_2 at megabar pressures

Prediction of high-pressure polymorphism in NiS$_2$ at megabar pressures

Yonggang G Yu and Nancy L Ross

Department of Geosciences, Virginia Polytechnic Institute and State University, Blacksburg, VA 24060, USA

E-mail: yuxxx135@umn.edu and nross@vt.edu

Abstract
A sequence of pressure-induced phase transitions of vaesite, NiS$_2$, with pyrite structure, has been established from static LDA calculations. A dozen AX$_2$ candidate structures have been studied at high pressures including cotunnite (α-PbCl$_2$), which is commonly observed in other AX$_2$ compounds at high pressures. At 150 GPa, vaesite transforms to a tetragonal phase ($P4_2/n$) rather than cotunnite. This tetragonal structure is characterized by layers of Ni atoms in eight-fold coordination with S atoms rather than the nine-fold coordination observed in cotunnite. With further compression to about 7.5 Mbar, the tetragonal phase transforms into a hexagonal AlB$_2$-type structure ($P6/mmm$) which is characterized by planar hexagonal layers of S intercalated by Ni atoms where each Ni atom is 12-fold coordinated by S atoms. Calculated band structures and valence electron density maps show S–S and Ni–S bonded interactions for NiS$_2$ under these extremely compressed conditions. The tetragonal phase may have geophysical implications if present in the Earth's core.

(Some figures in this article are in colour only in the electronic version)

1. Introduction

Vaesite, NiS$_2$, adopts the pyrite structure at ambient conditions and has been intensively studied over the past half century for its complex spin dynamics at low temperatures (e.g. [1–4]) and its insulator to metal transition induced either by pressure or by substituting S by Se (e.g. [5–8]). As shown in figure 1, NiS$_2$ is a paramagnetic charge transfer insulator at ambient conditions [9]. Upon cooling, it undergoes two consecutive magnetic transitions at 40 K (T_{N1}) and 30 K (T_{N2}), respectively. Neutron scattering experiments [1–3] have shown that a type-I antiferromagnetic (AF) state (spin aligned ferromagnetically within (001) plane, but antiferromagnetically ordered in consecutive planes) develops below T_{N1}, and that below T_{N2} both type-II AF state (spin aligned ferromagnetically within (111) plane, but antiferromagnetically ordered in consecutive planes) and a weak ferromagnetism coexist with the type-I AF state. Two types of symmetry-breaking patterns have been identified: one from cubic to tetragonal and the other from cubic to hexagonal. A spin chirality mechanism has been proposed to interpret the complex coexisting magnetic states with the accompanying lattice distortions, but needs to be confirmed by experiments [4]. At ambient conditions, the electronic structure of NiS$_2$ has been measured by

x-ray photo emission [9–11], and near-infrared and Raman studies have been reported [12, 13]. When compressed to higher pressures, NiS$_2$ displays an insulator to metal transition between 2 and 4 GPa [6] with a positive Clapeyron slope (figure 1). This insulator–metal transition can also be achieved by substitution of Se for S for which 10% Se substituted for S is equivalent to an approximately 1 GPa increase in pressure [6, 7]. The low-temperature AF metallic state ceases at ∼7 GPa (see two black dots on P axis in figure 1, one at 7 GPa reported from [6] and the other at 7.6 GPa being the most recent measurement [14]). The crystal structure evolution with pressure close to the insulator–metal transition point was also measured by single crystal x-ray diffraction (XRD) below 6 GPa [15]. A few DFT studies [16–22] have been reported for NiS$_2$ at ambient pressure. Among them, two GGA studies [17, 20] agree well with experiments in equilibrium lattice constant, but the nonmagnetic state obtained from GGA contradicts the AF insulating state determined from experiments at low temperatures. To the best of our knowledge, no experimental or theoretical studies have been reported on NiS$_2$ above 10 GPa.

Here we present the first ultrahigh pressure calculations of NiS$_2$. We report the sequence of phase transitions, and the
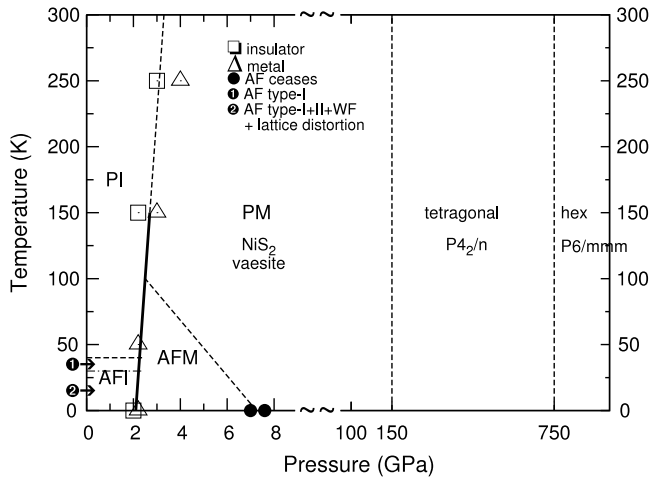
Figure 1. A tentative low-temperature and high-pressure phase diagram for NiS$_2$. All low pressure experimental data on insulator–metal transition are taken from [6] except the point (7.5 GPa, 0 K, from [14]) which ceases the AFM state. The phase diagram for the insulator–metal transition in Ni(S, Se)$_2$ system from [7, 67] was referred. A log scale is used above 100 GPa (P: paramagnetic, AF: antiferromagnetic, WF: weak ferromagnetic, M: metal, I: insulator, hex: hexagonal).

effect of pressure on crystal structures and the valence electron density distributions of the stable high-pressure polymorphs. In addition, we compare the high-pressure behavior of NiS$_2$ with that of other AX$_2$ compounds. Over the past two decades, pressure-induced phase transitions have been well established for groups of AX$_2$ compositions (see reviews in [23] and [24]). For example with increasing pressure, TiO$_2$ (group IVB dioxide) transforms from a rutile structure ($P4_2/mnm$) to the α-PbO$_2$ structure ($Pbcn$) to the baddeleyite structure (EuI$_2$-type, $P2_1/c$) to an orthorhombic-I structure (SrI$_2$-type, $Pbca$) and finally to the cotunnite (α-PbCl$_2$) structure ($Pnma$), while ZrO$_2$ and HfO$_2$ follow a similar route from baddeleyite to $Pbca$ to $Pnma$ (e.g. [25]). Group IVA oxides, such as SiO$_2$ and GeO$_2$, transform from the rutile structure to the CaCl$_2$ structure ($Pnnm$) to the α-PbO$_2$ structure to the pyrite structure (Pa-3), as demonstrated by experimental studies [26, 27], and finally to the cotunnite structure, as predicted by DFT calculations [28, 29]. Most cubic fluorite-type AF$_2$ compounds (A = Ca, Cd, Sr, Ba, Mn, Pb, and Eu) have been shown to transform to the cotunnite (α-PbCl$_2$) structure under high pressures [23]. The cotunnite structure is also observed as a high-pressure phase in actinide dioxides like UO$_2$ and ThO$_2$ [30] which at ambient pressure crystallize in the fluorite structure. Other compounds like CaCl$_2$, however, behave differently upon compression. It transforms to cotunnite, successively through α-PbO$_2$, EuI$_2$, and SrI$_2$ type phases. In all transitions described above, the coordination number of A gradually increases, reaching nine-fold coordination with surrounding X atoms in the cotunnite structure. Nonetheless, in some compounds, the cotunnite structure is found to transform with increasing pressure to other structures, such as the monoclinic $P2_1/a$ structure in PbCl$_2$ and SnCl$_2$ [31] and the inverse Ni$_2$In-type ($P6_3/mmc$) hexagonal structure in Na$_2$S [32], BaF$_2$ [33] and BaH$_2$ [34, 35].

It is clear from the above that many AX$_2$ compounds with widely varying compositions transform to a cotunnite structure with increasing pressure. This study, which is one of the few theoretical studies [36] of an AS$_2$ compound subjected to extreme pressure, explores whether a cotunnite structure also exists in NiS$_2$ or whether it undergoes a different structural evolution with pressure.

2. Method

We investigated the stability of NiS$_2$ in a number of candidate crystal structures (such as those described above) at high pressures using density functional theory (DFT) [37]. This study mainly uses Ceperley–Alder LDA [38] as parameterized by Perdew and Zunger [39] for exchange correlation functionals in combination with the plane wave pseudopotential method as implemented in the *Quantum ESPRESSO* package [40]. The S pseudopotential was generated by the [41] method using reference configuration 3s^{2}3p^{4}3d^0 (r_c = 1.70, 1.75, and 1.75 au for s, p, d channel, s local), whereas for Ni, an ultrasoft pseudopotential [42] was constructed from reference configuration 3d$^{7.75}$4s^{1}4p$^{0.25}$ with cutoff radius of 1.8 au for each quantum number l. The f state is chosen as the local potential with cutoff 1.8 au. Nonlinear core correction [43] is not used in S or Ni in pseudopotential generation. The cutoff energy is 80 and 500 Ryd for wavefunction and charge density Fourier expansion, respectively. These two pseudopotentials become unreliable above 800 GPa because the interatomic distance between S and Ni becomes smaller than the sum of valence electron wavefunction cutoff radii. To deal with pressures above 8 megabar (Mbar), we have generated another set of pseudopotentials with a smaller cutoff radius (details in appendix A.1). The Brillouin zone (BZ) integration was performed on Monkhorst–Pack k-point mesh [44] denser than $16 \times 16 \times 16$ (for all calculated phases especially at high pressures) together with the Methfessel and Paxton smearing method [45] with a smearing width of 0.003 Ryd to smooth up the Fermi surface.

To test the quality of the generated pseudopotential at high pressures, we calculated by LDA the unit cell parameter and equation of state of face centered cubic (fcc) ferromagnetic (FM) Ni as well as β-Po type, simple cubic (sc), and body centered cubic (bcc) sulfur. The static equilibrium lattice constant and bulk modulus of fcc FM Ni calculated from this study is within 1% difference compared with previous PAW LDA calculations [46]. We found that the magnetic moment of fcc-Ni vanishes at 6.1 Mbar within LDA, which agrees with the vanishing magnetic moment observed under compression from a previous GGA study [47]. Also our calculations reproduce previous calculations of cell parameter variation of β-Po type sulfur with pressure and on the static transition pressure between the sc and bcc phase in sulfur (550 GPa by LDA) [48, 49]. Crystal structures are relaxed under hydrostatic pressures using variable cell shape molecular dynamics [50–52]. The spin polarized LDA yields a nonmagnetic state for NiS$_2$ vaesite at all pressures, which is in agreement with the previous GGA study [19] and consistent with the experimental observation at high pressures that vaesite
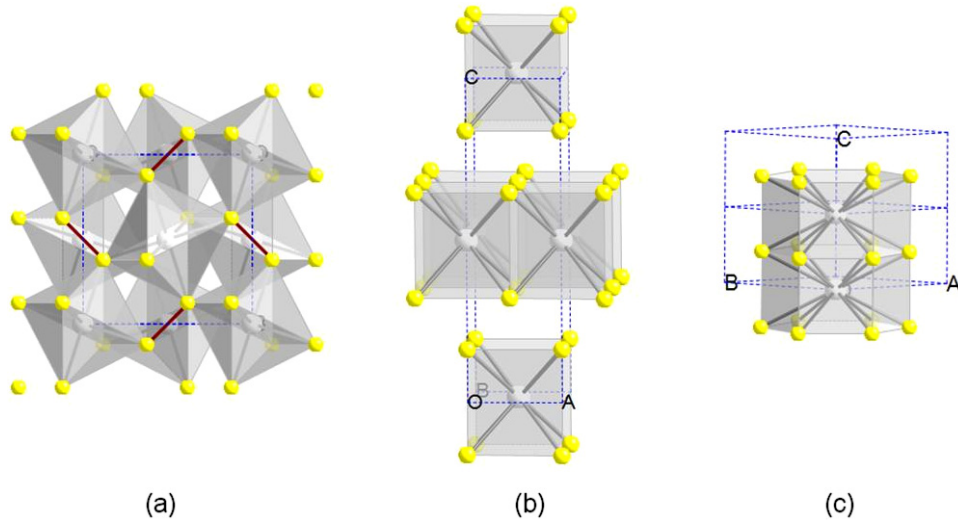
Figure 2. Crystal structure of NiS$_2$ cubic vaesite at ambient condition (a), tetragonal $P4_2/n$ phase at 150 GPa (b), and AlB$_2$ hexagonal $P6/mmm$ phase at 750 GPa (c). Nickel atoms are shown as gray spheres and sulfur as yellow. (Their structure parameters are shown in table 2.)
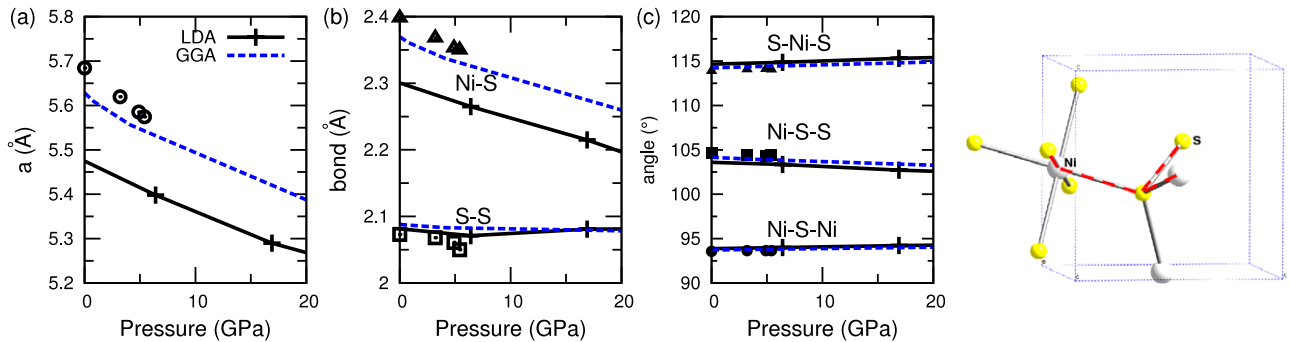
Figure 3. Evolution with pressure of vaesite NiS$_2$ lattice constant (a), n.n. distances of S–S and Ni–S (b), and some selected angles (c). Straight lines connecting '+' signs are LDA results and the dashed lines are from PBE-GGA. Circles, triangles, and squares represent single crystal x-ray diffraction data at room temperature up to 5.4 GPa [15]. All bonds and angles are defined within a cluster of five atoms delineated by red lines on the right, where sulfur atoms are in yellow spheres and nickel in gray.

is paramagnetic above 8 GPa (figure 1). The PBE-GGA [53] results on vaesite are also shown, but the difference in valence electron density from the two functionals is negligible and the GGA transition pressures between vaesite, the tetragonal phase, and the hexagonal phase are less than 20 GPa higher than those by the LDA. Thus we report chiefly the LDA results.

3. Results and discussion

Our investigation of the high-pressure structural evolution of vaesite, with the pyrite structure, has found that three phase transitions occur above 100 GPa. At 150 GPa vaesite transforms to a predicted tetragonal structure ($P4_2/n$). With further compression to about 7.5 Mbar, the tetragonal phase transforms into a hexagonal AlB$_2$-type structure ($P6/mmm$). Below, we describe the structure, equations of state, compression mechanism, electronic band structure, and features of the valence electron density isosurface of the three stable phases of NiS$_2$ found with increasing pressure: vaesite, the tetragonal phase, and the hexagonal phase (figure 2).

We then describe some of the metastable structures that emerged from molecular dynamics simulations of baddeleyite and cotunnite. A comparison is made with phase transitions observed in other AX$_2$ compounds.

3.1. Stable high-pressure phases of NiS$_2$

3.1.1. Vaesite. The crystal structure of vaesite at 150 GPa is shown in figure 2(a). Vaesite is isostructural with pyrite, with Ni atoms sitting in the centers of the faces of a cube and with S atoms intercalated to form NiS$_6$ octahedra that tilt consecutively around [001] in four different directions. Within an octahedron, the first and second nearest neighbor (n.n.) Ni–S distances are 2.0 and 2.1 Å, respectively. An S$_2$ dimer is observed with a short S–S distance of 1.98 Å, thus if one looks at the coordination of sulfur-centered polyhedra, each sulfur atom is tetrahedrally coordinated by three Ni atoms and one S atom (figure 3).

Figure 3(a) shows the evolution with pressure of the unit cell parameter of vaesite calculated by LDA and GGA at 0 GPa without including zero point motions in comparison with
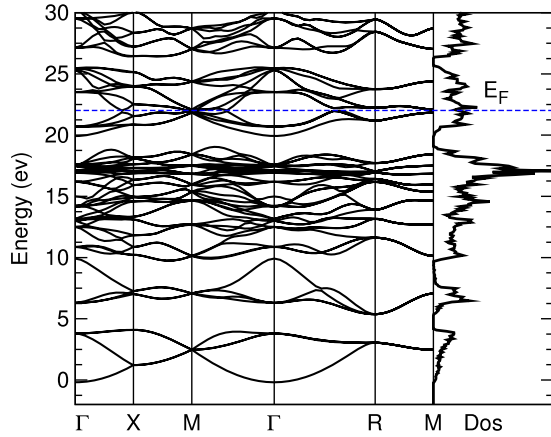
Figure 4. Electronic band structure of vaesite NiS_2 at 147 GPa. X: (1/2, 0, 0), M: (1/2, 1/2, 0), and R: (1/2, 1/2, 1/2) in units of $2\pi/a$.

Table 1. LDA static equation of states of nonmagnetic NiS_2 polymorphs (see figure 2) at 0 GPa and 0 K (without zero point motion).

| Phase	Volume ($\mathring{A}^3$/f.u.)	K_0 (GPa)	K_0'
Vaesite (LDA)[a]	41.04	132.85	4.55
Vaesite (GGA)	44.58[b], 44.81[c], 46.05[d]	102.1[b]	4.6[b]
Vaesite (exp.)	45.92[e]	133.2 ± 5.2[f]	5.73 ± 0.58[f]
$P4_2/n$[a]	40.33	101.04	4.34
AlB_2[a]	40.21	97.12	4.33

[a] This work LDA. [b] This work with PBE-GGA.
[c] Reference [19] with GGA [66]. [d] Reference [20] with PW91.
[e] Reference [15] single crystal XRD at room condition.
[f] FeS_2 pyrite, powder XRD [55].

the experiment at 300 K [15]. The GGA static compression curves agree better with experiments than the LDA ones, which underestimate by ∼4% the unit cell parameter as well as the n.n. Ni–S distance at ambient pressure. This can be attributed to: (1) LDA overbinds atoms and GGA underbinds them as is well known, (2) the zero point motion and 300 K thermal contribution (from phonons) to lattice expansion are absent in the static calculation, and (3) both LDA and GGA predict a metallic state at 0 K rather than the insulating state observed at 300 K from experiments (figure 1). Nevertheless, the LDA, GGA, and XRD data agree on the pressure dependence of n.n. S–S distance and angles formed between S–Ni–S, Ni–S–S, and Ni–S–Ni, as highlighted in red dashed lines in a skeleton structure in figure 3. We found in the LDA calculation a slight decrease in the S–S dimer distance with compression from 0 to 6 GPa and then a slight increase at higher pressures (figure 3). The GGA calculation gives a monotonic decreasing S–S distance with pressure. The room temperature XRD S–S distance appears to have a dip around 4.6 GPa [15], which was used to interpret the incipience of the insulator–metal transition. However, it is not clear from the XRD data whether the insulator to metal transition is weakly first order or second order [54].

Simulations were performed up to 300 GPa and, as expected, the static LDA equilibrium volume is 10.6%
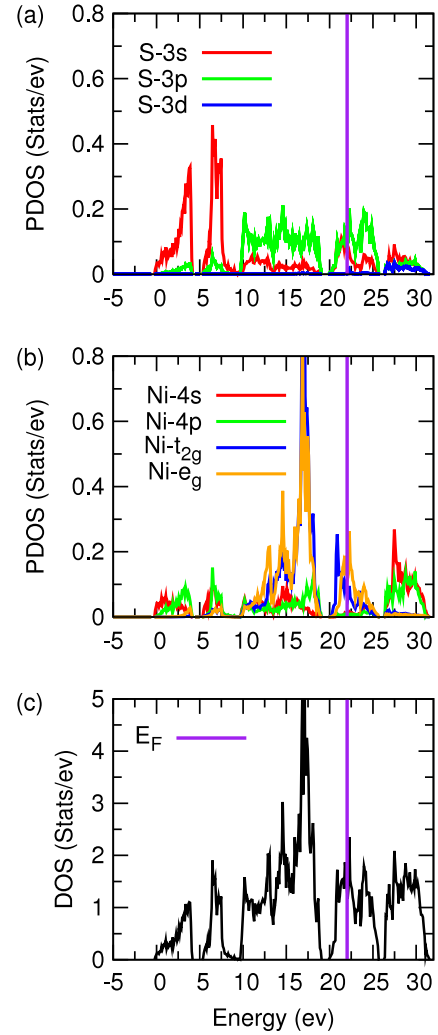

Figure 5. Projected density of states of vaesite NiS_2 at 147 GPa.

lower than the experimental value at 300 K (table 1). Our GGA calculation agrees well with previous static GGA calculations [17, 20] and measurements at room conditions [15] on volume and the unit cell parameter. The calculated static bulk modulus and its pressure derivative for vaesite obtained from fitting the LDA volume versus pressure data with a third order Birch–Murnaghan equation of state are 132.9 GPa and 4.6, respectively. These values are similar to the experimental values of pyrite, FeS_2, which has an isothermal bulk modulus, $K_T = 132.2 \pm 5.2$ GPa, and a pressure derivative, K_T of 5.7 ± 0.6 [55].

Figure 4 shows the LDA electronic band structure of NiS_2 vaesite at 147 GPa. It resembles that of FeS_2 pyrite at high pressures [56]. The two broad peaks centered around 4 and 7 eV arise from tight binding of sulfur 3s states. Bands between 10 and 20 eV are formed by mixing of sulfur 3p and Ni 3d states, which is clearly seen from the projected density of states (figure 5). The appearance of some Ni 4p states below the Fermi surface is surprising. The Fermi level runs across the Ni 3d states and S 3p states, showing a metallic feature. The crystal field splitting of t_{2g} and e_g bands in the octahedral environment is not correctly accounted for by
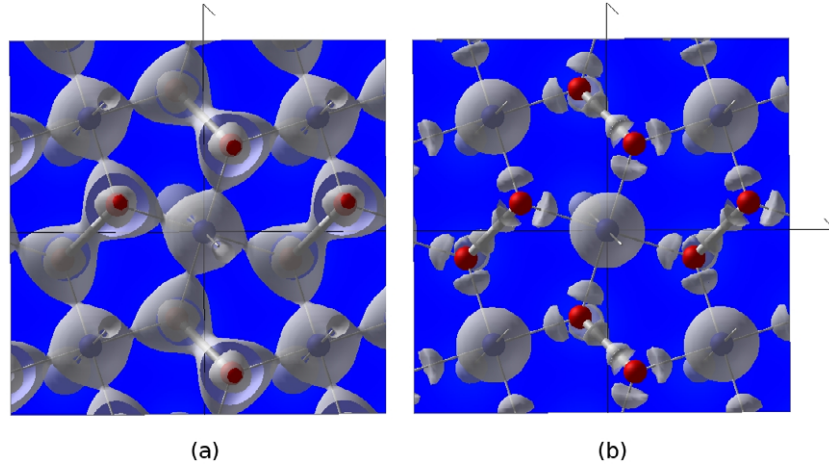
Figure 6. Isosurface of valence electron density of vaesite NiS$_2$ at 147 GPa: 0.98e Å^{-3} (a) and 1.19e Å^{-3} (b). Red spheres represent sulfur atoms and blue nickel atoms.
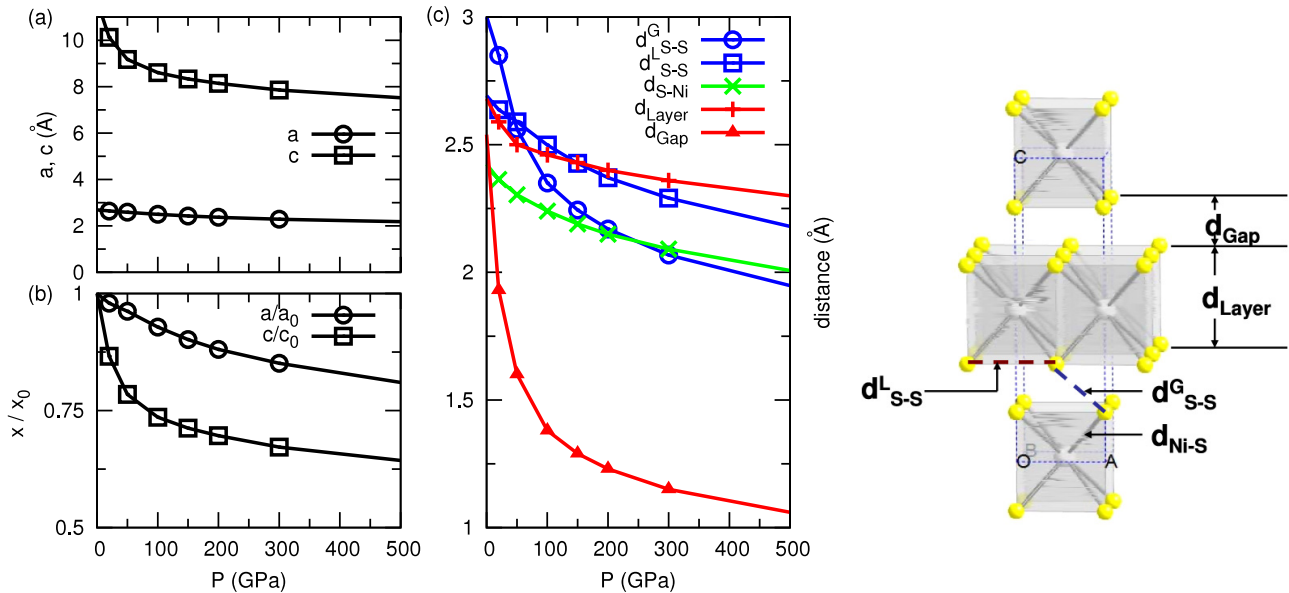

Figure 7. Evolution of the cell parameters and bond lengths with pressure in $P4_2/n$ NiS$_2$. Nickel is shown by gray spheres and sulfur by yellow spheres.

LDA. The mixing between S 3p and Ni 3d states can also be seen from the valence electron isosurface map (figure 6). At relatively low density (0.98e Å^{-3}), charge accumulations between Ni and S exhibit sphere and bell-connected shapes, and charge accumulations between the nearest neighbor S$_2$ dimer show a dumbbell shaped surface. At a higher charge density value, such as 1.19e Å^{-3}, the S–S 3p-σ type molecular bonds and S 3p and Ni 4s interactions are manifested by cone-like charge distributions around the S–S and Ni–S bonds. The existence of a S$_2$ dimer in vaesite, a solid state crystal, is remarkable and clearly visualized from the charge density isosurface (figure 6).

3.1.2. Tetragonal ($P4_2/n$) polymorph of NiS$_2$. Vaesite, the ambient pressure stable phase, is predicted to transform at 150 GPa (LDA, 152 GPa by PBE-GGA) to a layered tetragonal

structure with $P4_2/n$ symmetry which is more stable than cotunnite. The layers in the tetragonal phase consist of face-sharing NiS$_8$ tetragonal prisms formed by S atoms with Ni in the center. The Ni–S distance within the prisms is 2.19 Å at 150 GPa. Here the Ni is in eight-fold coordination with S rather than in the nine-fold coordination as in cotunnite. These layers stack in a zigzag fashion perpendicular to the c axis (figure 2(b)). When compressed from ambient pressure to 100 GPa, c decreases sharply from 11.7 to 8.6 Å, but the a parameter within the layer decreases only from 2.7 to 2.5 Å (figure 7(a)). At 100 GPa the c/c_0 and a/a_0 ratios, where c_0 and a_0 are the values at 0 GPa, are 0.73 and 0.94, respectively, indicating that the c axis is much softer than the a axis (figure 7(b)). This can be attributed to the weaker S–S interaction between layers, which also results in a sharp reduction of the inter-layer distance (d_{Gap}) and of the S–S distance within the gap (d_{S-S}^G) (figure 7(c)). On the other
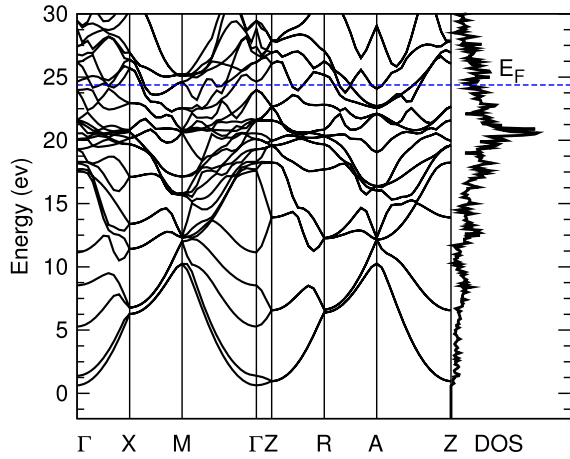
Figure 8. Electronic band structure of $P4_2/n$ NiS$_2$ at 150 GPa. X: $(1/2, 0, 0)$, M: $(1/2, 1/2, 0)$, Z: $(0, 0, a/2c)$, R: $(1/2, 0, a/2c)$, and A$(1/2, 1/2, a/2c)$ in units of $2\pi/a$.

hand, the thickness of the NiS$_8$ layer (d_{Layer}) and the S–Ni distance within the layer (d^L_{S-Ni}) decrease very slowly from 0 to 500 GPa (figure 7(c)). These compressional trends imply that the Ni–S bonds are stiffer than the S–S bonds. Above 100 GPa the tetragonal structure becomes notably less compressible, suggesting that repulsive forces between the layers contribute to the overall compressibility of the structure (figure 7(c)). Owing to the initial softness perpendicular to the tetragonal layers in the $P4_2/n$ phase, the static bulk modulus and its pressure derivative at ambient pressure are 101 GPa and 4.3, respectively, both of which are smaller than those of vaesite (table 1).

Figure 8 shows the LDA band structure and total density of states of the tetragonal phase at 150 GPa. The lower energy bands from 0 to 10 eV retain some tight binding features from sulfur s atomic orbitals. However, the higher energy bands from 15 to 30 eV are more complex than those found for vaesite. The Fermi level cuts across the valence bands. The projected density of states show that sulfur 3p and nickel 3d orbitals overlap between 15 and 25 eV (figure 9). This suggests that when forming crystals, the tetragonal NiS$_8$ prisms may experience strong p–d electron hybridization, thus neither p nor d orbitals can be preserved. Moreover, the tetragonal crystal field splitting in 3d orbitals of nickel is absent in LDA (figure 9(b)). Figure 10 shows the valence electron charge density isosurface. At a low charge density, such as 0.43e Å^{-3} (figure 10(a)), we clearly see charge accumulation between Ni–Ni atoms which comes from outer shell electrons such as 4s. Also observed is charge accumulation within sulfur layers, presumably from outer s electrons. At a higher valence charge density of 1.17e Å^{-3} (figure 10(b)) the nearest neighbor S–S interaction seems to attract electrons into a cage-shaped distribution, where electrons are accumulated along [1 1 1] pointing towards the first n.n. S atoms, but depleted along [1 0 0] towards second nearest neighbors. We suspect that the lack of atomic s or p shape charge density around sulfur atoms results from band mixing in the environment of the tetragonal prism formed by sulfur and nickel atoms which is also seen from the complex band structure near the Fermi level (figure 8).
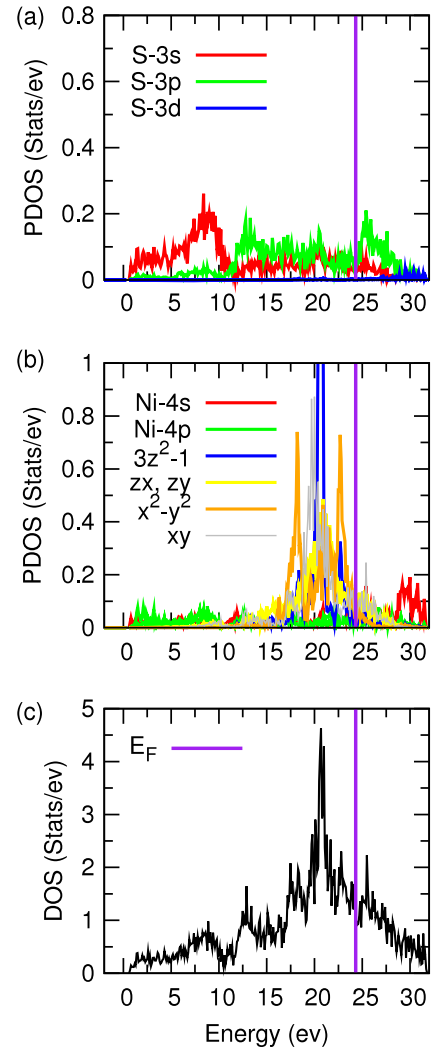

Figure 9. Projected density of states of $P4_2/n$ NiS$_2$ at 150 GPa.

3.1.3. Hexagonal (P6/mmm) polymorph of NiS$_2$. The LDA calculations indicate that tetragonal phase of NiS$_2$ transforms to a hexagonal phase with $P6/mmm$ symmetry above 750 GPa (770 GPa by PBE-GGA) which is isostructural with AlB$_2$. The most commonly observed post-cotunnite phase in AX$_2$ systems is the hexagonal inverse-Ni$_2$In-type ($P6_3/mmc$) structure first observed in BaF$_2$ [33]. This structure has since been verified to occur as a post-cotunnite phase in Na$_2$S [32] and BaH$_2$ [34]. Recently Kinoshita *et al* [35] observed a phase transition in BaH$_2$ from the inverse-Ni$_2$In-type structure to a simple hexagonal phase between 50 and 65 GPa, but the symmetry of this new structure was not determined. They, however, proposed it was an AlB$_2$-type structure.

Figure 2(c) shows the crystal structure of the AlB$_2$-type hexagonal NiS$_2$ calculated at 800 GPa. It consists of face-sharing NiS$_{12}$ hexagonal prisms stacked parallel to the c direction. In contrast to the tetragonal phase where Ni was in eight-fold coordination with S, Ni is in 12-fold coordination with neighboring S atoms in the hexagonal structure. The n.n. Ni–S and S–S distances are 2.012 and 1.787 Å, respectively. The n.n. Ni–Ni distance is 1.849 Å, which is comparable to 1.943 Å, the Ni–Ni distance in metallic fcc-Ni at 800 GPa
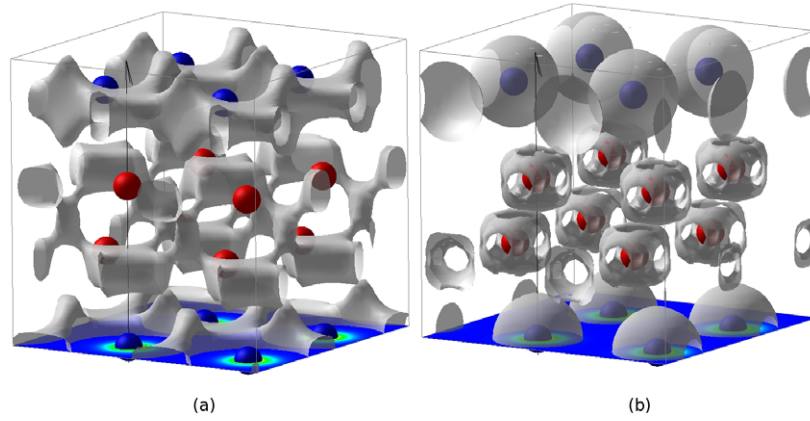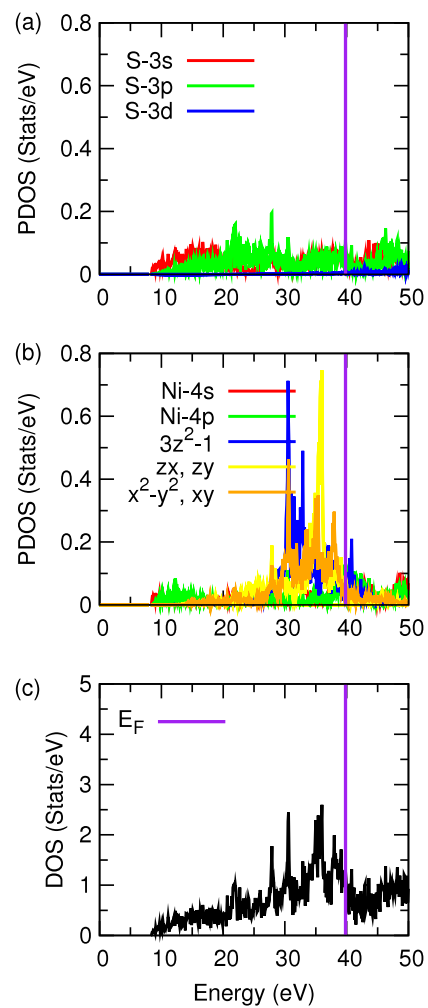
Figure 10. Isosurface of valence electron density of $P4_2/n$ NiS$_2$ at 150 GPa: 0.43e Å^{-3} (a) and 1.17e Å^{-3} (b). Red spheres represent sulfur atoms and blue spheres nickel atoms.
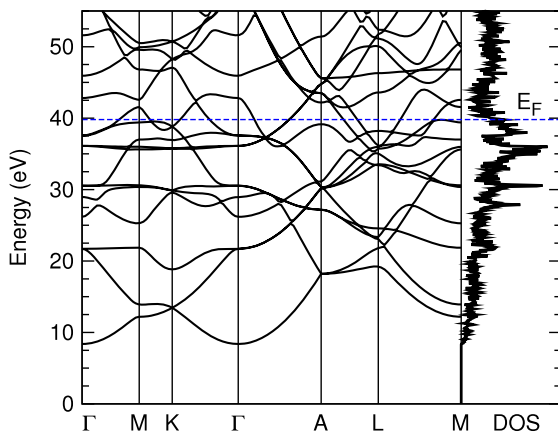
Figure 11. Electronic band structure of AlB$_2$-type NiS$_2$ at 800 GPa. M: (1/2, 0, 0), K: (1/2, 1/2$\sqrt{3}$, 0), A: (0, 0, $\sqrt{3}a/4c$), and L: (1/2, 0, $\sqrt{3}a/4c$) in units of $4\pi/\sqrt{3}a$.

Figure 12. Projected density of states of AlB$_2$-type NiS$_2$ at 800 GPa.

(LDA from this work). The static bulk modulus and its pressure derivative for the AlB$_2$ phase at 0 GPa are 97.1 GPa and 4.33, respectively (table 1), close to the values of tetragonal NiS$_2$.

The electronic structure and the density of states of AlB$_2$-type NiS$_2$ calculated at 800 GPa are shown in figure 11 and the projected density of states are shown in figure 12. The Fermi level cuts across the bands showing metallic features. The lowest energy bands, occurring along the Γ–M–K–Γ direction that are within the hexagonal plane, consist of bonding and antibonding states of S 3p-σ orbitals, closely resembling those of two-dimensional graphite [57]. The valence electron charge density isosurface map is shown in figure 13. The Ni–Ni interaction comprises σ-bonds within the hexagonal layer and ring-like π-bond features between two adjacent Ni layers (with charge density of 0.69e Å^{-3}, figures 13(a) and (b)). At a charge density of 1.35e Å^{-3} (figures 13(c) and (d)), the S–S 3p-σ orbitals (bone-shaped) form hexagonal rings connecting sulfur atoms within the hexagonal plane, meanwhile the S–S 3p$_z$ orbitals (dumbbell shaped) connect the two adjacent sulfur layers. The Ni PDOS shows overlap between projected s and p states by hybridization (figure 12) which may give rise to the appearance of ring-shaped isosurface above Ni atoms.

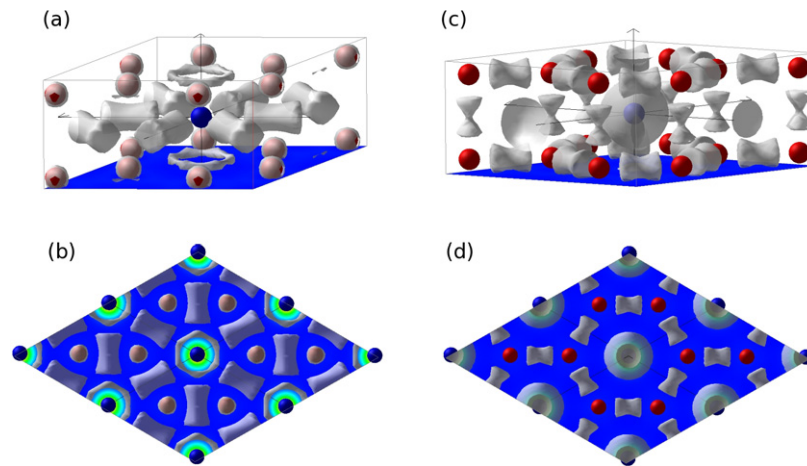Similar s and p hybridizations forming 3p-σ and 3p$_z$ orbitals are expected within and in between sulfur layers.
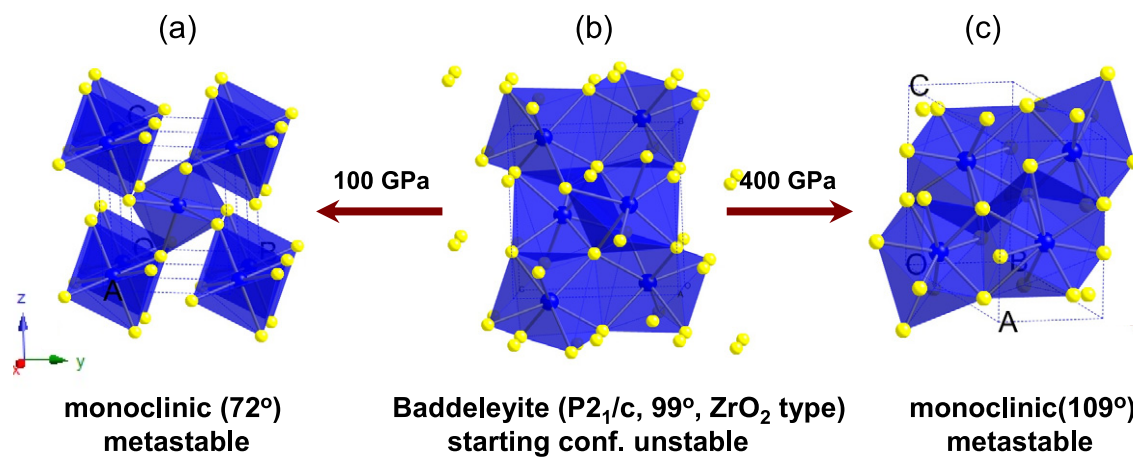
3.2. Metastable structures of NiS$_2$

In searching for high-pressure phases of NiS$_2$, we encountered a few new structures obtained from molecular dynamics

Figure 13. Isosurface of valence electron density of AlB$_2$-type NiS$_2$ at 800 GPa: $0.69e$ Å^{-3} ((a) front view and (b) topview) and $1.35e$ Å^{-3} ((c) front view and (d) top view). Red spheres represent sulfur atoms and blue spheres nickel atoms.


Figure 14. Starting from ZrO$_2$ baddeleyite-type ($P2_1/c$) configuration in NiS$_2$ (b), two metastable structures were obtained—(a) monoclinic structure ($P2_1/n$) with an angle 72° at 100 GPa and (c) cotunnite-like monoclinic structure ($P2_1/c$) with an angle 109° at 400 GPa.

simulations at various pressures starting from different initial structures. Although the new structures are metastable, they are of interest as they reveal distinct aspects of the high-pressure behavior of NiS$_2$ compared to dioxides which may be applicable to studies of other disulfides subjected to extreme pressures.

3.2.1. Evolution with pressure of NiS$_2$ with baddeleyite structure. Baddeleyite ($P2_1/c$) is the stable phase under ambient conditions for ZrO$_2$ and other IVB dioxides such as HfO$_2$ [58]. In this structure, each metal atom is coordinated by seven oxygen atoms [59]. This monoclinic structure is also an intermediate high-pressure phase for TiO$_2$, which undergoes the transition from rutile → α-PbO$_2$ → baddeleyite → the orthorhombic-I phase ($Pbca$, SrI$_2$) → cotunnite ($Pnma$) (e.g. [25]). The baddeleyite phase is absent in SiO$_2$ and GeO$_2$ at high pressure, which instead follow a sequence of transitions from rutile → CaCl$_2$ ($Pnnm$, marcasite) → α-PbO$_2$ → pyrite [26, 27]. DFT calculations indicate that a further transition to cotunnite happens at ∼700 GPa in SiO$_2$ [28, 29]. It is important to compare these results with the predicted phase transition sequence in NiS$_2$ at high pressures, not only to

elucidate the effect of S substituting for O in AX$_2$ compounds, but also to build a framework for understanding and predicting phase transitions in AX$_2$ groups as a whole.

We therefore started with NiS$_2$ in a baddeleyite structure determined from experiments [59] (figure 14) and subjected it to various pressures between 0 and 500 GPa. Upon decreasing pressure below 100 GPa, the system relaxes into a monoclinic structure which resembles marcasite in which NiS$_6$ octahedra share corners with each other (figure 14(a)) and the monoclinic angle is ∼72°. On the other hand, when this baddeleyite structure is subjected to high pressures in excess of 400 GPa, it evolves into a distorted monoclinic cotunnite-like structure in which each Ni atom is bonded to nine S atoms (figure 14(c)) and the monoclinic angle is 108°. Between 100 and 400 GPa, the baddeleyite structure is difficult to optimize under hydrostatic pressure. Although we were able to stabilize the marcasite- and cotunnite-like structures from the high-pressure simulations, they are both found metastable as their volume and static internal energy are both greater than those of the tetragonal phase ($P4_2/n$) between 100 and 500 GPa. Thus the baddeleyite-type structure in NiS$_2$ is unstable at all pressures. The structure evolution, as shown in figure 14, suggests that six-fold coordinated structures (such as pyrite
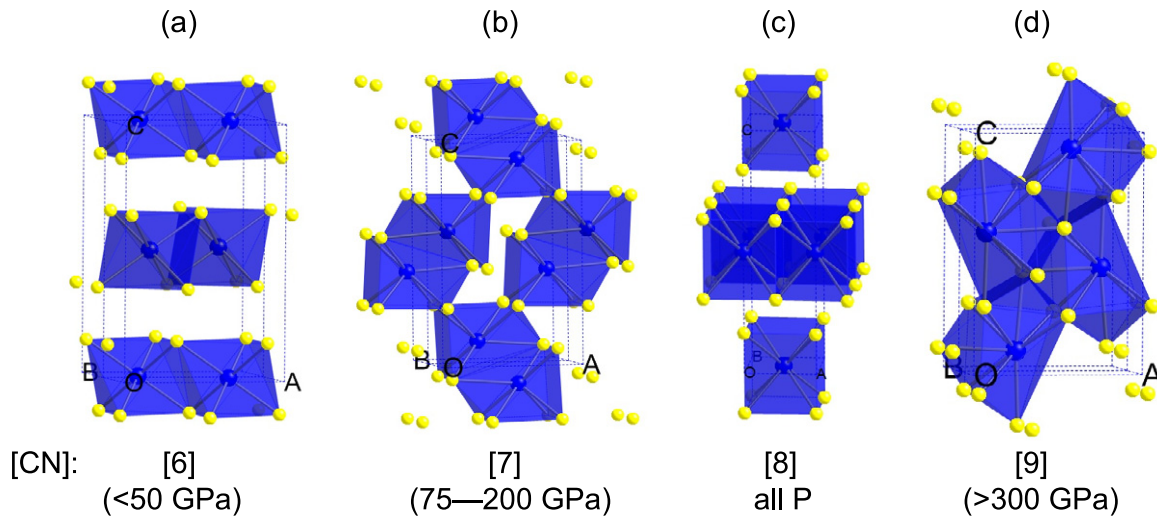
Figure 15. Cotunnite related NiS$_2$ structures obtained from structural relaxation at various pressures. (a) A layered structure with edge-sharing SiO$_6$ octahedra under 50 GPa, (b) a layered structure with edge-sharing SiO$_7$ units stable from 75 to 200 GPa, (c) tetragonal layered structure ($P4_2/n$) stabilized at all pressures, (d) nine-fold coordinated cotunnite structure stable above 300 GPa ($Pnma$). CN stands for coordination number.

and marcasite) are more favorable below 100 GPa, while nine-fold coordinated structures related to cotunnite appear more favorable above 400 GPa. In order to explore other high-pressure phases of NiS$_2$, we started directly from the cotunnite structure as described below.

3.2.2. Evolution with pressure of NiS$_2$ with cotunnite type structure. Structural relaxations of NiS$_2$ with a ZrO$_2$-type cotunnite structure [59] at a series of pressures from 0 to 8 Mbar yield four candidates for high-pressure polymorphs of NiS$_2$ (figure 15). At pressures less than 50 GPa, we find a layered structure formed by edge-sharing NiS$_6$ octahedra resembling the structure of TiS$_2$ (isostructure with CdI$_2$, figure 15(a)). At intermediate pressures from 75 to 200 GPa, an edge-sharing NiS$_7$ layered structure appears (figure 15(b)). This seven-bond coordinated structure differs from baddeleyite (figure 14(b)). Above 300 GPa, the nine-fold coordinated cotunnite structure emerges (figure 15(d)), which remains stable to higher pressures. Surprised at the spontaneous inversion of cotunnite structure into six- and seven-coordinated structures, we recompressed these two layered structures to 75 GPa (figure 15(a)) and find, after re-optimization, the layered tetragonal structure (figure 15(c)) with $P4_2/n$ symmetry, described in section 3.1.2. This tetragonal structure is attainable at all pressures and dynamically stable (see phonon dispersion in appendix A.2). Although it has not been reported before, the occurrence of layered structures in AX$_2$ compounds at high pressure is well known. For example, the inverse-Ni$_2$In-type hexagonal layered structure was found as a post-cotunnite phase in compounds such as BaH$_2$. In addition, the WSe$_2$- (MoS$_2$-) type trigonal layered structure [60, 61] has recently been reported as a post-cotunnite phase in WN$_2$ [62]. To distinguish the stability fields of the observed phases, we compare their static energy versus volume curves in figure 16, where cotunnite is shown by open squares, the tetragonal phase by open circles, the seven-fold coordinated

phase by diamonds, the six-fold coordinated layered phase by triangles, and the vaesite phase by the solid red line. At small volumes (high pressures), energies of the cotunnite and the tetragonal phase are very close and much lower than that of vaesite, indicating vaesite must transform under compression to structures with higher coordination numbers. However the energetics of cotunnite and the tetragonal phase are too close at high pressure to allow for comparison. Instead we compare enthalpy versus pressure of vaesite and the tetragonal phase relative to that of cotunnite phase above 300 GPa (because the cotunnite phase is only stable above 300 GPa from simulation). Figure 16(b) shows that the tetragonal phase is the most stable one from 300 up to ~750 GPa. The cotunnite structure is only 0.02 Ryd/formula greater in enthalpy than the tetragonal phase at 300 GPa and the enthalpy difference between them decreases with compression. Owing to uncertainties in k-point sampling and Gaussian-smearing near the Fermi surface, current accuracy in static energy is about 5 mRyd/formula which is close to enthalpy differences between the two structures at 600 GPa. Therefore an estimated transition pressure from tetragonal to cotunnite phase would be 750 ± 150 GPa if no other phase intervened. However, we found that the AlB$_2$-type hexagonal phase ($P6/mmm$) is more stable than both the tetragonal and cotunnite phases above ~750 GPa, which is consistent with known post-cotunnite structures such as AlB$_2$ and inverse-Ni$_2$In type (e.g. [23]).

3.3. Additional metastable phases of NiS$_2$

The previous sections show the three stable phases as well as metastable structures encountered in NiS$_2$ during structure optimization under compression. We also investigated a number of other crystal structures with AX$_2$ composition at high pressures. As shown above, baddeleyite transforms into two monoclinic structures depending on pressure. The monoclinic ($P2_1/a$) phase observed in PbCl$_2$ and SnCl$_2$ [31] relaxes into a different monoclinic structure with edge-sharing octahedra (see appendix A.3). The orthorhombic
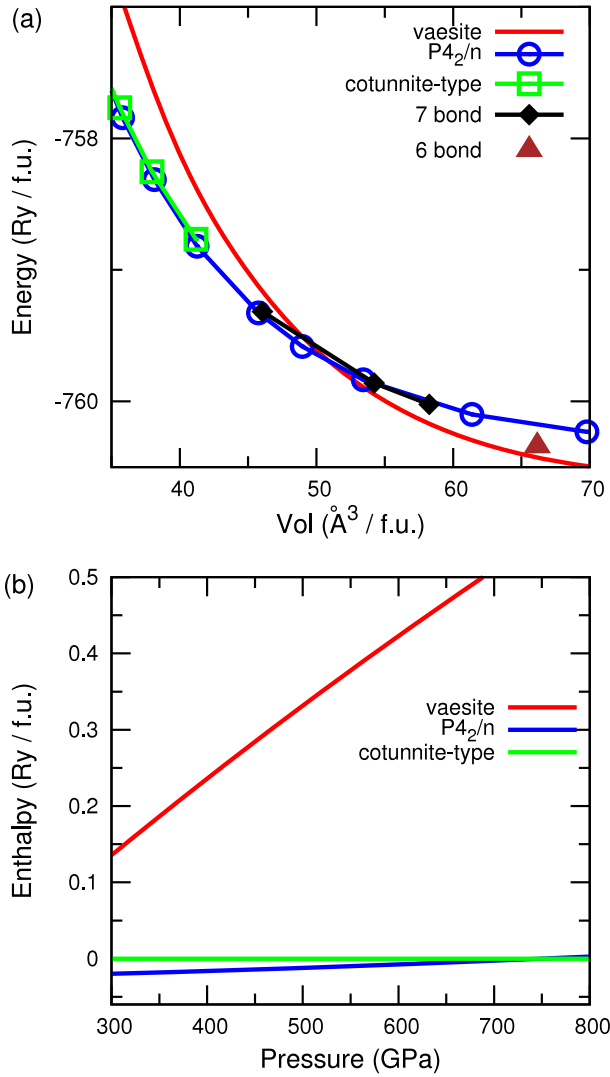
Figure 16. Energetics of cotunnite related structures as shown in figure 15. (a) Energy versus volume curves for vaesite, the tetragonal phase, cotunnite (stable above 300 GPa), and layered seven-bond and six-bond coordinated structures (within 200 GPa). (b) Enthalpy versus pressure curves for vaesite, tetragonal, and cotunnite above 300 GPa.

Table 2. Cell parameters (in Å) of various NiS₂ structures from simulations. CN stands for coordination number.

CN = 6			
Vaesite	Pa-3 (205)	Cubic	40 GPa
(a, a, a)	5.13		
Ni (4a)	0	0	0
S (8c)	0.3828 (0.3955[a])	0.3828	0.3828
Marcasite	*Pnnm* (58)	Orthorhombic	50 GPa
(a, b, c)	4.2429	5.1281	3.0968
Ni (2a)	0	0	0
S (4g)	0.1825	0.3814	0
α-PbO₂	*Pbcn* (60)	Orthorhombic	50 GPa
(a, b, c)	4.0451	5.9152	5.6440
Ni (4c)	0	0.1311	1/4
S (8d)	0.1956	0.4005	0.4504
WSe₂	*P6₃/mmc* (194)	Hexagonal	150 GPa
(a, b, c)	2.2662	2.2662	11.1668
Ni (2d)	1/3	2/3	1/4
S (4e)	1/3	2/3	0.593
			(0.621[b])

CN = 8			
Flourite	*Fm̄3m* (225)	Cubic	0.5 GPa
(a, a, a)	5.556		
Ni (4a)	0	0	0
S (8c)	1/4	1/4	1/4
Newly found	*P4₂/n* (86, origin 1)	Tetragonal	150 GPa
(a, b, c)	2.3707	2.3707	8.1439
Ni (2b)	0	0	0.5
S (4f)	0	0	0.1653

CN = 9			
Cotunnite	*Pnma* (62)	Orthorhombic	400 GPa
(a, b, c)	4.89	2.25	6.87
Ni (4c)	0.361	0.25	0.079
S (4c)	0.396	0.25	0.406
S (4c)	0.124	0.75	0.268
CmSe₂	*P4/nmm* (129 origin 1)	Orthorhombic	200 GPa
(a, b, c)	2.8514	2.8514	5.8439
Ni (2c)	1/2	0	0.3075
S (2a)	0	0	0
S (2c)	1/2	0	0.6452

CN = 12			
Ni₂In (inverse)	*P6₃/mmc* (194)	Hexagonal	200 GPa
(a, b, c)	3.5221	3.5221	4.3684
Ni (2c)	1/3	2/3	1/4
S (2a)	0	0	0
S (2d)	1/3	2/3	3/4
AlB₂	*P6/mmm* (191)	Hexagonal	800 GPa
(a, b, c)	3.0956	3.0956	1.8486
Ni (1a)	0	0	0
S (2d)	1/3	2/3	1/2

[a] Exp. [15]. [b] Reference [60].

(*Imma*) phase of MgB₂-type [63] reverts to the AlB₂-type structure. The remaining high-pressure candidates of NiS₂ investigated include structures with (i) six-fold coordination of Ni with S: marcasite (*Pnnm*), α-PbO₂ (*Pbcn*), WSe₂ (*P6₃/mmc*, isostructural with WS₂ and MoS₂); (ii) eight-fold coordination of Ni with S: cubic fluorite (*Fm̄3m*); (iii) nine-fold coordination of Ni with S: CmSe₂-type structure (*P4/nmm*), α-PbCl₂ cotunnite (*Pbnm*) mentioned above; and (iv) 12-fold coordination of Ni with S: hexagonal inverse-Ni₂In-type (*P6₃/mmc*), and simple hexagonal AlB₂-type (*P6/mmm*) [61]. The relaxed unit cell parameters and fractional coordinates are shown in table 2.

To further simplify comparison, metastable phases are ignored and a few structures are neglected. The nine-fold coordinated CmSe₂ structure, for example, is less stable than the cotunnite structure. Figure 17(a) shows enthalpy of 10 high-pressure candidate polymorphs of NiS₂ (including two

assemblages of Ni(fcc) plus S(sc) and S(bcc), respectively) from 0 to 400 GPa in comparison with that of vaesite. Other than the CaF₂ phase, all other phases have lower enthalpies (i.e., more stable) than vaesite between 150 and 300 GPa. Vaesite is the most stable phase from 0 to 150 GPa, before the tetragonal phase becomes more stable with a volume reduction of ∼9% at the transition. Figure 17(b) compares the enthalpies
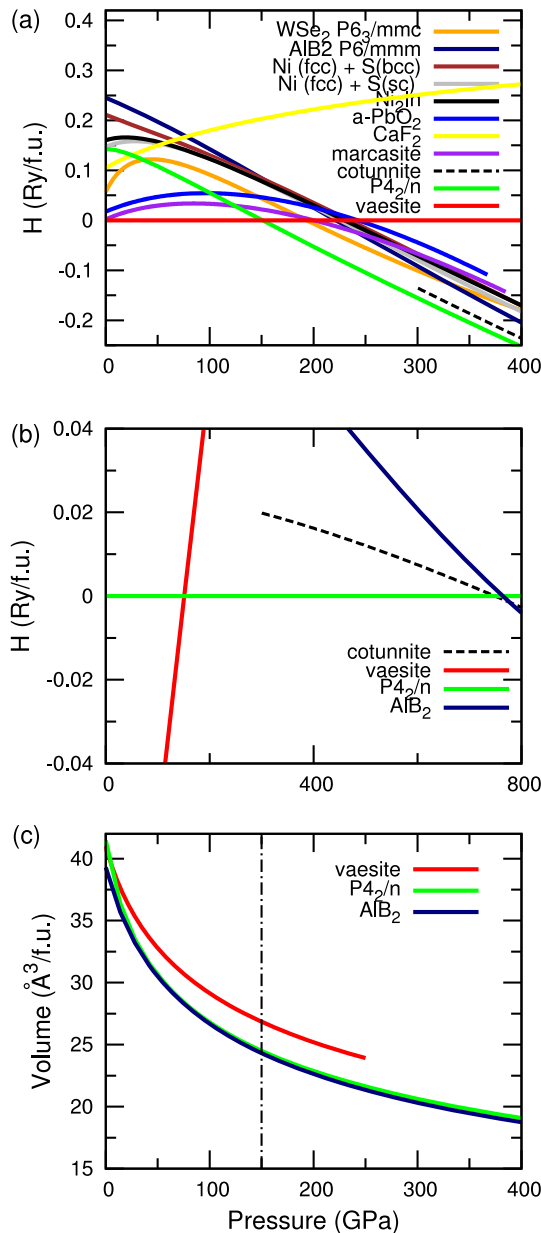
Figure 17. Static enthalpy of various NiS$_2$ structures up to 400 GPa (a); enthalpy of vaesite, the tetragonal ($P4_2/n$), cotunnite, and the hexagonal AlB$_2$ ($P6/mmm$) up to 800 GPa (b); volume versus pressure equation of states of NiS$_2$ vaesite, tetragonal, and hexagonal phases up to 400 GPa (c).

of vaesite, the cotunnite phase, and the hexagonal AlB$_2$ phase, all relative to the tetragonal phase. Above ∼750 GPa, NiS$_2$ with the cotunnite structure becomes more favorable than the tetragonal phase, but it is less stable than the AlB$_2$ phase. The AlB$_2$ hexagonal phase takes the place of the tetragonal phase at about 750 GPa. Figure 17(c) shows the volume–pressure equation of state of vaesite, the tetragonal, and the hexagonal phase.

4. Conclusion

A tentative low-temperature phase diagram for NiS$_2$ is summarized in figure 1. The high-pressure phase transitions

in NiS$_2$ from vaesite to the layered tetragonal phase to the layered hexagonal phase follow the general trend in pressure-induced transitions: an increase in coordination number from 6 to 8 to 12, respectively, accompanied by a substantial decrease in volume at the transition. At 150 GPa the volume reduction from vaesite to the tetragonal phase is ∼9% and that from the tetragonal to the AlB$_2$ hexagonal phase is ∼1.5% at 750 GPa. The charge density isosurface maps clearly reveal charge accumulation between S–S dimers in vaesite, cage-shaped isosurface for S in the tetragonal phase, and S–S bonded interactions within and between sulfur layers and Ni–Ni bonded interactions in the hexagonal AlB$_2$ phase.

As seen in figure 17(b), the enthalpies of the tetragonal, cotunnite, and the hexagonal phase nearly cross the same point near 750 GPa. Due to uncertainties in computing static energy of metallic systems, we are unable to rule out the existence of the cotunnite phase in NiS$_2$ at high pressures. Nevertheless, the dominance of the tetragonal phase from 150 GPa to about 750 GPa is conclusive. The phase transition trend established here in NiS$_2$, from vaesite, to the newly predicted tetragonal phase, to the AlB$_2$ phase, suggests that layer segregation and element accretion in Ni and S play a dominant theme at high pressures. Whether this reflects the molecular nature of sulfur is unknown. The ubiquitous observation of cotunnite phase in AX$_2$ compositions including oxides such as, SiO$_2$ [28, 29], GeO$_2$ [26, 27], ZrO$_2$ and HfO$_2$ [59, 64], TiO$_2$ [25], halides such as BaF$_2$ [33, 65], chlorides such as PbCl$_2$ and SnCl$_2$ [31], and hydrites such as BaH$_2$ [34, 35], but not in NiS$_2$ might be attributed to the same molecular nature in sulfur which disfavors the irregular bonding as in cotunnite, but prefers layered structures. Further high-pressure studies on sulfides are needed to clarify this conjecture. In addition, the effect of van der Waals interactions on the phase transition needs to be explored.

Another possibility raised from this molecular dynamics study is that amorphization may occur before the transition of vaesite to the tetragonal phase. As described above, many metastable structures were encountered in the simulation. Among these, the metastable monoclinic structure with layered edge-sharing NiS$_6$ prisms (figure 15(a)) are about 70 meV/atom higher in enthalpy than the tetragonal phase at 150 GPa and might occur under non-hydrostatic pressure or at high temperature, e.g., above ∼1000 K. Experiments are needed to confirm the high-pressure behavior of NiS$_2$.

The layered tetragonal and hexagonal structures may be prototypes of high-pressure phases in other AS$_2$ sulfides, such as FeS$_2$. If present in the Earth, the tetragonal phase may have implications for transport and elastic properties owing to its structural anisotropy.

Acknowledgments
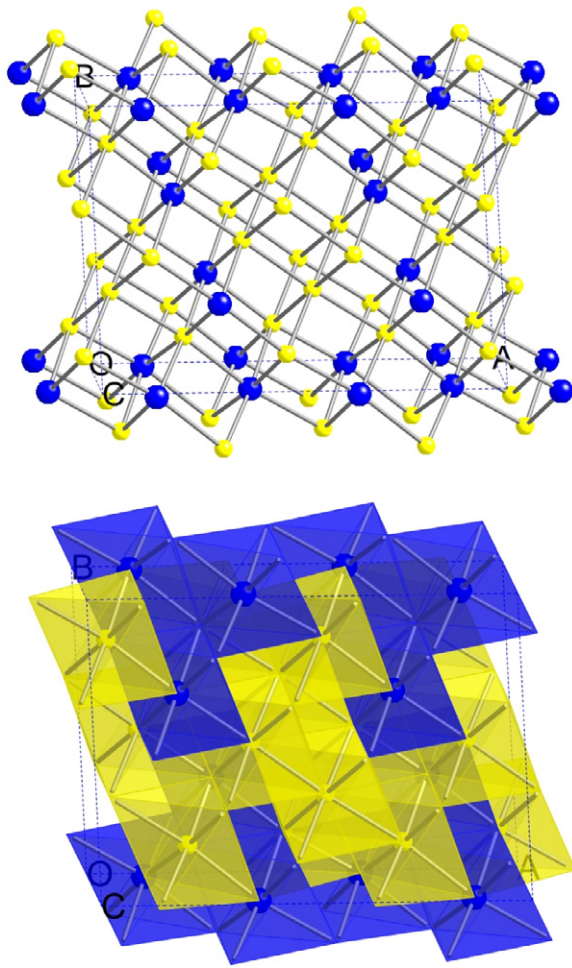
Figure A.1. Illustration of one metastable structure in NiS$_2$ with congested sulfur networks obtained from simulation at 100 GPa starting with a $P2_1/a$-type structure (PbCl$_2$ [31]). Yellow spheres represent sulfur atoms and blue spheres nickel.

Appendix

A.1. Pseudopotential at high pressure

A second S pseudopotential was generated by the [41] method using reference configuration $3s^23p^43d^0$ (r_c = 1.5 au for s, p, and d channel, s local). A second Ni ultrasoft pseudopotential [42] was constructed from reference configuration $3d^{7.75}4s^14p^{0.25}$ with cutoff radius of 1.5 au for each quantum number l. The f state is chosen as the local potential with cutoff 1.5 au. The wavefunction cutoff is 500 Ryd and charge density cutoff is 2000 Ryd [29]. K-point mesh and smearing parameters are the same as described in the method section. The equation of state of FCC FM Ni is reproduced and the sc-bcc transition pressure in sulfur is found to be 500 GPa rather than 550 GPa as in a previous study [49].

A.2. Phonon of the tetragonal phase

The $P4_2/n$ tetragonal NiS$_2$ is found dynamically stable. The phonon dispersion and vibrational density of states at 300 GPa is shown in figure A.2.
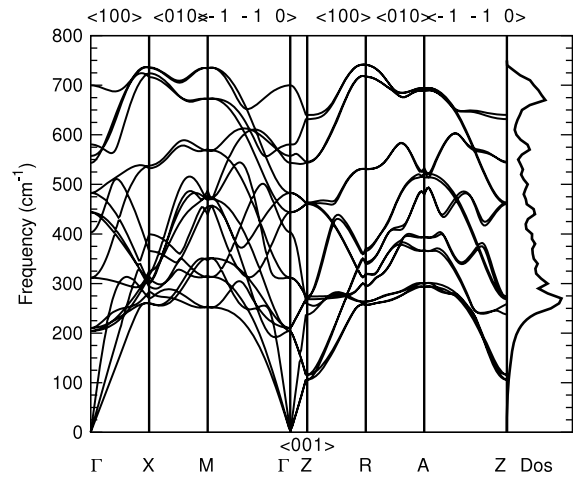
Figure A.2. Phonon dispersion and vibrational density of states of the NiS$_2$ tetragonal phase ($P4_2/n$) at 300 GPa.

A.3. A metastable structure

When $P112_1/a$ (PbCl$_2$ [31]) phase was taken as the initial configuration, relaxation at 100 GPa yields one structure where both nickel and sulfur atoms intercalate, but more aggregated sulfur and nickel clusters form (figure A.1).

References

[1] Miyadai T, Takizawa K, Nagata H, Ito H, Miyahara S and Hirakawa K 1975 *J. Phys. Soc. Japan* **38** 115
[2] Thio T, Bennett J W and Thurston T R 1995 *Phys. Rev.* B **52** 3555
[3] Matsuura M, Endoh Y, Hiraka H, Yamada K, Mishchenko A S, Nagaosa N and Solovyev I V 2003 *Phys. Rev.* B **68** 094409
[4] Shindou R and Nagaosa N 2001 *Phys. Rev. Lett.* **87** 116801
[5] Wilson J A 1985 *The Metallic and Nonmetallic States of Matter* ed P P Edwards and C N R Rao (London: Taylor and Francis) pp 215–60
[6] Sekine Y, Takahashi H, Môri N, Matsumoto T and Kosaka T 1997 *Physica* B **237** 148
[7] Miyasaka S, Takagi H, Sekine Y, Takahashi H, Môri N and Cava R 2000 *J. Phys. Soc. Japan* **69** 3166
[8] Husmann A, Brooke J, Rosenbaum T F, Yao X and Honig J M 2000 *Phys. Rev. Lett.* **84** 2465
[9] Fujimori A, Mamiya K, Mizokawa T, Miyadai T, Sekiguchi T, Takahashi H, Môri N and Suga S 1996 *Phys. Rev.* B **54** 16329
[10] Matsuura A Y, Shen Z X, Dessau D S, Park C H, Thio T, Bennett J W and Jepsen O 1996 *Phys. Rev.* B **53** R7584
[11] Mamiya K, Mizokawa T, Fujimori A, Miyadai T, Chandrasekharan N, Krishnakumar S R, Sarma D D, Takahashi H, Môri N and Suga S 1998 *Phys. Rev.* B **58** 9611
[12] de las Heras C and Agulló-Rueda F 2000 *J. Phys.: Condens. Matter* **12** 5317
[13] Scrocco M 1998 *J. Electron. Spectrosc. Relat. Phenom.* **94** 237
[14] Niklowitz P G, Alireza P L, Steiner M J, Lonzarich G G, Braithwaite D, Knebel G, Flouquet J and Wilson J A 2008 *Phys. Rev.* B **77** 115135
[15] Fujii T, Tanaka K, Marumo F and Noda Y 1987 *Miner. J. Japan* **13** 448
[16] Temmerman W M, Durham P J and Vaughan D J 1993 *Phys. Chem. Miner.* **20** 248
[17] Raybaud P, Kresse G, Hafner J and Toulhoat H 1997 *J. Phys.: Condens. Matter* **9** 11085

[18] Raybaud P, Hafner J, Kresse G and Toulhoat H 1997 *J. Phys.: Condens. Matter* **9** 11107
[19] Hobbs D and Hafner J 1999 *J. Phys.: Condens. Matter* **11** 8197
[20] Wang J H, Cheng Z, Brédas J L and Liu M 2007 *J. Chem. Phys.* **127** 214705
[21] Gibbs G V, Downs R T, Prewitt C T, Rosso K M, Ross N L and Cox D F 2005 *J. Phys. Chem. B* **109** 21788
[22] Gibbs G V, Cox D F, Rosso K M, Ross N L, Downs R T and Spackman M A 2007 *J. Phys. Chem. B* **111** 1923
[23] Leger J M and Haines J 1997 *Eur. J. Solid State Inorg. Chem.* **34** 785
[24] Manjón F J and Errandonea D 2009 *Phys. Status Solidi* b **246** 9
[25] Dubrovinskaia N A, Dubrovinsky L S, Ahuja R, Prokopenko V B, Dmitriev V, Weber H P, Osorio-Guillen J M and Johansson B 2001 *Phys. Rev. Lett.* **87** 275501
[26] Prakapenka V B, Dubrovinsky L S, Shen G, Rivers M L, Sutton S R, Dmitriev V, Weber H P and Bihan T L 2003 *Phys. Rev. B* **67** 132101
[27] Ono S, Tsuchiya T, Hirose K and Ohishi Y 2003 *Phys. Rev. B* **68** 134108
[28] Oganov A R, Gillan M J and Price G D 2005 *Phys. Rev. B* **71** 064104
[29] Umemoto K, Wentzcovitch R M and Allen P B 2006 *Science* **311** 983
[30] Idiri M, LeBihan T, Heathman S and Rebizant J 2004 *Phys. Rev. B* **70** 014113
[31] Leger J M, Haines J and Atouf A 1996 *J. Phys. Chem. Solids* **57** 7
[32] Vegas A, Grzechnik A, Syassen K, Loa I, Hanfland M and Jansen M 2001 *Acta Crystallogr. B* **57** 151
[33] Leger J M, Haines J, Atouf A, Schulte O and Hull S 1995 *Phys. Rev. B* **52** 13247
[34] Smith J S, Desgreniers S, Tse J S and Klug D D 2007 *J. Appl. Phys.* **102** 043520
[35] Kinoshita K, Nishimura M, Akahama Y and Kawamura H 2007 *Solid State Commun.* **141** 69
[36] Wu X, Steinle-Neumann G, Qin S, Kanzaki M and Dubrovinsky L 2009 *J. Phys.: Condens. Matter* **21** 185403
[37] Kohn W and Sham L J 1965 *Phys. Rev.* **140** 1133
[38] Ceperley D M and Alder B J 1980 *Phys. Rev. Lett.* **45** 566
[39] Perdew J P and Zunger A 1981 *Phys. Rev. B* **23** 5048
[40] Giannozzi P *et al* 2009 *J. Phys.: Condens. Matter* **21** 5502
[41] Troullier N and Martins J L 1991 *Phys. Rev. B* **43** 1993
[42] Vanderbilt D 1990 *Phys. Rev. B* **41** 7892
[43] Louie S G, Froyen S and Cohen M L 1982 *Phys. Rev. B* **26** 1738
[44] Monkhorst H J and Pack J D 1976 *Phys. Rev. B* **13** 5188
[45] Methfessel M and Paxton A T 1989 *Phys. Rev. B* **40** 3616
[46] Dewaele A, Torrent M, Loubeyre P and Mezouar M 2008 *Phys. Rev. B* **78** 104102
[47] Černý M, Pokluda J, Šob M, Friák M and Šandera P 2003 *Phys. Rev. B* **67** 035116
[48] Zakharov O and Cohen M L 1995 *Phys. Rev. B* **52** 12572
[49] Rudin S P and Liu A Y 1999 *Phys. Rev. Lett.* **83** 3049
[50] Wentzcovitch R M, Martins J L and Price G D 1993 *Phys. Rev. Lett.* **70** 3947
[51] Wentzcovitch R M 1991 *Phys. Rev. B* **44** 2358
[52] Parrinello M and Rahman A 1981 *J. Appl. Phys.* **52** 7182
[53] Perdew J P, Burke K and Ernzerhof M 1996 *Phys. Rev. Lett.* **77** 3865
[54] Imada M, Fujimori A and Tokura Y 1998 *Rev. Mod. Phys.* **70** 1039
[55] Merkel S, Jephcoat A P, Shu J, Mao H-K, Gillet P and Hemley R J 2002 *Phys. Chem. Miner.* **29** 1
[56] Cai J, Goliney I and Philpott M R 2006 *J. Phys.: Condens. Matter* **18** 9151
[57] Saito R, Dresselhaus G and Dresselhaus M S 1998 *Physical Properties of Carbon Nanotubes* (London: Imperial College Press)
[58] Wang J, Li H P and Stevens R 1992 *J. Mater. Sci.* **27** 5397
[59] Desgreniers S and Lagarec K 1999 *Phys. Rev. B* **59** 8467
[60] Wyckoff R W G 1963 *Crystal Structures I* 2nd edn, vol 1 (New York: Interscience)
[61] Rao C N R and Pisharody K P R 1976 *Prog. Soid State Chem.* **10** 207
[62] Wang H, Li Q, Li Y, Xu Y, Cui T, Oganov A R and Ma Y 2009 *Phys. Rev. B* **79** 132109
[63] Ma Y, Wang Y and Oganov A R 2009 *Phys. Rev. B* **79** 054101
[64] Liu L-G 1980 *J. Phys. Chem. Solids* **41** 331
[65] Wu X, Qin S and Wu Z 2006 *Phys. Rev. B* **73** 134103
[66] Perdew J P, Chevary J A, Vosko S H, Jackson K A, Pederson M R, Singh D J and Fiolhais C 1992 *Phys. Rev. B* **46** 6671
[67] Iwaya K, Kohsaka Y, Satow S, Hanaguri T, Miyasaka S and Takagi H 2004 *Phys. Rev. B* **70** 161103(R)

13